Disentangling ionic and electronic contributions to the switching dynamics of memristive $Pr_{0.7}Ca_{0.3}MnO_3$/Al devices by employing a two-resistor model

Alexander Gutsche,* Sebastian Hambsch, Nuno Casa Branca, and Regina Dittmann†
Forschungszentrum Juelich GmbH, PGI-7, 52425 Jülich, Germany

Stefan Scholz and Joachim Knoch
IHT, RWTH Aachen University, 52056 Aachen, Germany

(Received 17 May 2022; revised 4 July 2022; accepted 19 July 2022; published 21 September 2022)

Area-dependent memristive devices such as Al/$Pr_{0.7}Ca_{0.3}MnO_3$ (PCMO) stacks are highly interesting candidates for synapses in neuromorphic circuits due to their gradual switching properties, their reduced variability and the possibility to tune the resistance with the device area. However, due to the complexity of the different processes taking place, the electronic and ionic transport in theses devices is so far only poorly understood and physical compact models to simulate their behavior are missing so far. We developed a mathematical description of the dynamics of theses devices based on a simple two-resistor model that reproduces the device behavior very well. Based on x-ray photoelectron spectroscopy and impedance spectroscopy we assign the two resistors to the AlO_x layer and a depletion zone at the $Pr_{0.7}Ca_{0.3}MnO_3$ layer, respectively. We assign the parameters used within the mathematical model to physical parameters and make use of them in order to explain the dynamics of the switching processes during the SET and RESET process in different voltage regimes. For both poly- and single crystalline PCMO thin film devices, oxygen migration between the AlO_x and the PCMO depletion zone is responsible for the resistance change. However, the dynamics differ significantly due to the increased mobility of oxygen vacancies with increasing defect density in the case of the polycrystalline samples. Moreover, we observe volatile subloops in our current-voltage curves, which vanish within millisecond time scale. Based on our two-resistor model and the band diagram derived from spectroscopic measurements, we assign these subloops to the injection of electrons into traps within the AlO_x barrier.

DOI: 10.1103/PhysRevMaterials.6.095002

I. INTRODUCTION

Today's memristive devices are highly promising candidates to overcome the limits of conventional nonvolatile memory, such as flash memory, due to their high scalability, low power consumption and simple structure. Moreover, memristive devices might be employed as hardware representation of synapses in neuromorphic circuits. Memristive devices can be firstly classified by their switching mechanism, namely valence change mechanism (VCM) [1,2] or electrochemical metalization (ECM) [3,4]. Whereas ECM cells are always switching along nanosized filaments, VCM devices can switch both filamentary as well as across the whole device area [2,5].

The latter type of VCM device shows a clear scaling of the current with the device area for both low resistive state (LRS) and high resistive state (HRS), which offers more degrees of freedom for circuit design compared to filamentary systems. Due to the different switching kinetics, area-dependent devices exhibit both a gradual SET and RESET process [6–8]. This is in contrast to filamentary devices that usually show only a gradual RESET but a sharp SET process that renders the adjustment of multilevel switching more difficult [9,10]. Due to the well-defined multilevel switching resulting from the gradual switching process, area-type VCM devices are highly interesting for analog computing and as synapse in neural networks.

One promising candidate for area dependent resistive switching devices is $Pr_{0.7}Ca_{0.3}MnO_3$ (PCMO) in combination with a tunnel barrier or a native oxide formed at the interface to an oxidizable metal layer [11]. Although there is a common agreement that oxygen drift and diffusion is the underlying mechanism in these devices, the complex material stack, with sublayers that are all very sensitive to the oxygen content, makes it difficult to assign changes of the resistance to a change in the oxygen concentration within a certain sublayer at a given applied voltage [7,12–17]. A simulation of the switching process within these devices becomes even more complicated since a variety of electronic transport mechanisms come into play inside the different sublayers such as Poole-Frenkel emission [18,19], direct tunneling [20,21], trap-assisted tunneling [21,22], as well as polaron hopping [23], which all result in a complex nonlinear current-voltage dependence [7,24]. Therefore, so far no realistic physical models exist that sufficiently describe the dynamics of area-dependent PCMO-based devices.

To close the gap, we developed a mathematical model, consisting of two serial resistors to describe the I-V

*a.gutsche@fz-juelich.de
†r.dittmann@fz-juelich.de

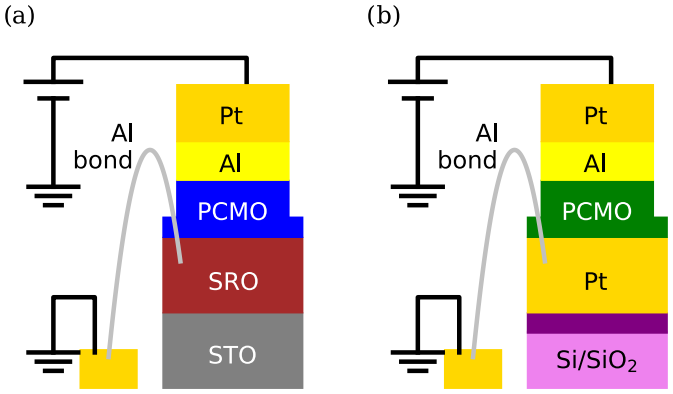

FIG. 1. The schematics of the sample stacks, using SC (a), blue) and PC (b), green) PCMO. The thicknesses of the thin films are: (a) 30 nm $SrRuO_3$ (SRO), 15 nm $Pr_{0.7}Ca_{0.3}MnO_3$ (PCMO), 7 nm Al, 20 nm Pt, and (b) 25 nm Pt bottom electrode, 20 nm PCMO, 7 nm Al, 25 nm Pt top electrode. The bottom electrode is always on ground, and the voltage polarizes the top electrode.

characteristics of PCMO/Al devices after biasing with different voltage amplitudes. Based on x-ray photoelectron spectroscopy and impedance spectroscopy we assign the two resistors to the AlO_x layer and a depletion zone at the $Pr_{0.7}Ca_{0.3}MnO_3$ layer, respectively. Based on this, we assign the parameters used within the mathematical model to physical parameters and make use of it in order to explain the dynamics of the switching processes during the SET and RESET process in different voltage regimes. Additionally, we investigate volatile states, so called subloops and explain their behavior within the framework of our model.

This model enables us to identify the physical processes that dominate the switching process and to simulate the dynamics of the resistance change of PCMO/Al devices. Moreover, this model could be used as input for circuit design in the field of neuromorphic computing in the future.

II. EXPERIMENTAL

A. Sample preparation

We compare two different types of devices, based on single crystalline (SC) and polycrystalline (PC) PCMO, as depicted in Figs. 1(a) and 1(b), respectively. For the SC samples, we grow the SC films on a SC $SrTiO_3$ (STO) substrate from SHINKOSHA. We etch the STO substrate for 3 min 30 s in buffered HF acid to remove the surface Sr in order to get a Ti termination. Afterwards, we anneal the STO for 2 h at 950 °C, to smooth out the surface after etching. The substrate has a step-terrace structure with a step-terrace length of 143 nm.

We use 30 nm $SrRuO_3$ (SRO) as the bottom electrode. We grow the bottom electrode using pulsed laser deposition (PLD), at 650 °C and 0.133 mbar O_2 partial pressure. The laser is an Eximer KrF-Laser with a wavelength of 248 nm. The repetition rate is 5 Hz and the energy density 3.0 J cm^{-2}. We monitor the growth process *in situ* with reflection high energy electron diffraction (RHEED), and confirm the step-flow growth mode of SRO.

We deposit the 20 nm $Pr_{0.7}Ca_{0.3}MnO_3$ (PCMO) directly afterwards under 0.133 mbar O_2 partial pressure and at 700 °C. The repetition rate is 5 Hz and the energy density is 1.7 J cm^{-2}. The RHEED measurement confirms a layer-by-layer growth of the PCMO. After the growth, the sample is cooled down with 10 °C/min in 226 mbar of O_2 partial pressure.

For the PC samples, a 25 nm-thick Pt film serves as bottom electrode. It was sputtered on top of a 5 nm Ta adhesion layer on a thermally oxidized Si wafer. On top, a 20 nm PCMO film is grown by pulsed laser deposition (PLD) at room temperature and 1.33 J cm^{-2}. Afterwards, the sample was annealed for two minutes at 650 °C in N_2 atmosphere to crystallize the amorphous PCMO film. XRD patterns of both PCMO thin films to prove the single and polycrystalline nature of the films can be found in the Supplemental Material [25].

After the PLD growth of SC and PC PCMO, we remove the samples from the PLD chamber and use e-beam evaporation to deposit 7 nm of Al and 20 nm of Pt *in situ*. As a result of the heat evolution during the evaporation process, the samples are heated up to 180 °C.

We structure the samples into quadratic pads with 100 μm, 50 μm, 20 μm, and 10 μm edge length, using photo lithography. We etch the samples with an Ar-ion beam down into the PCMO layer and remove the photoresist with DMSO afterwards.

We glue the samples with silver paste or carbon pads on a larger SiO_2 chip with 1×1 μm^2 Pt pads. We bond with Al wires through the PCMO and connect the bottom electrodes with the Pt pad on the SiO_2 chip. Figure 1 shows the complete sample stacks with electrical connections for both types of samples.

B. Instruments

The electrical measurements are performed with a Keithley 2611B (I-V-measurements) and a Keithley 4200 (pulse measurements). The XPS measurements are performed with a VersaProbe system from Physical Electronics.

III. RESULTS

A. XPS measurements

Prior to the device electrical characterisation, we perform x-ray photoelectron spectroscopy (XPS) measurements to gain information about the chemical state and the band alignment of our SC and PC Al/PCMO system. We investigate bare, SC/PC PCMO and PCMO with 7 nm of Al evaporated on it. We measure at a take-off angle of 30° and 80° to get depth information about the chemical state of the Al film.

Figure 2(a) shows the min to max normalized spectrum of the Al 2p region. At both angles, the spectrum consists of a main peak at 73 eV binding energy (BE) and a much smaller shoulder at 75 eV BE. The main peak belongs to the metallic Al [26]; the shoulder belongs to the oxidized Al. The inset shows a zoomed in version of the region that can be assigned to the presence of AlO_x contribution at different take-off angles. It can be seen that for a higher take-off angle, the intensity of the oxide signal increases.

Since XPS measurements at small take-off-angles are much more surface sensitive than measurements at higher take-off-angles [27] we can conclude that the AlO_x forms at the interface to the PCMO and not at the surface.

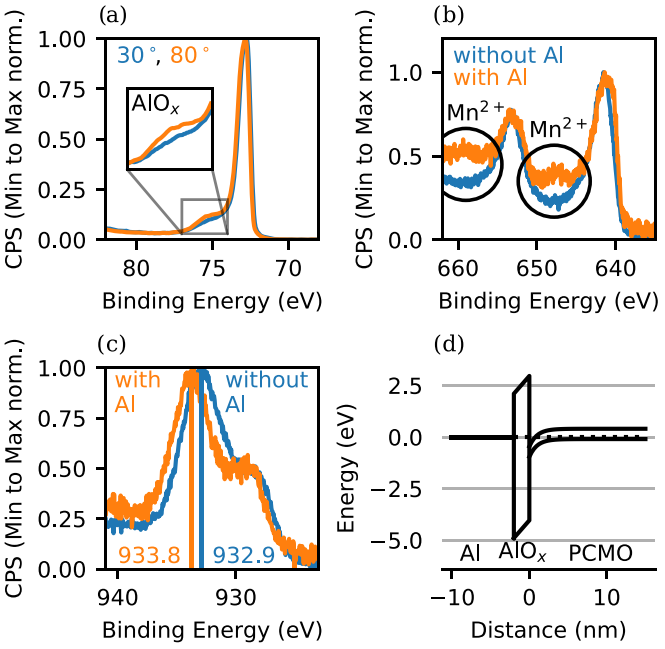

FIG. 2. (a) Spectrum of the Al $2p$ region of a SC sample. The big peak belongs to the metallic Al. The inset shows the angle dependence of the oxidized Al. (b) Spectrum of the Mn $2p$ region. In blue the bare PCMO; in orange the PCMO with Al evaporated on top. The circles indicate the formation of the Mn^{2+} satellites. (c) The spectrum of the Pr 3d 5/2 region. In blue the bare PCMO; in orange the PCMO with Al evaporated on top. The vertical lines show the peak shift between the measurements. (d) The band diagram constructed from the XPS measurements.

Figure 2(b) shows the spectrum of the Mn $2p$ region with its doublets at 641 eV and 653 eV BE. The blue line belongs to the pure PCMO; the orange line belongs to the PCMO with evaporated Al on top. Mn is present in PCMO in two different oxidation states: Mn^{3+} and Mn^{4+} [24]. However, shake-up satellites appear after the deposition of Al. These shake-up satellites only appear when Mn^{2+} is present [28]. Additionally, the Pr 5/2 peak shifts to slightly lower BEs. Both observations show the oxygen loss of PCMO after the deposition of Al.

We conclude, that the deposited Al pulls out the oxygen from the PCMO. This reduces the PCMO and oxidizes the Al locally at the interface.

Figure 2(c) shows the spectrum of the Pr $3d$ region. The blue line belongs to the pure PCMO; the orange line belongs to the PCMO with evaporated Al on top. The peak of the Mn $3d$ 5/2 peak shifts from 932.9 eV to 933.8 eV BE when Al is deposited. The BE is referenced to the Fermi energy of the system. Therefore, the increase in binding energy indicates a downward band bending when Al is deposited.

Figure 2(d) shows the band structure reconstructed from the XPS measurements. The position of the valence band edge of the AlO_x is calculated from the position of the Al $2p$ orbital of the oxidized Al. For corundum, the valence band edge lies at -4 eV and the $2p$ peak at -74.14 eV. In our measurements the position of the $2p$ orbital is at -75 eV and therefore the valence band edge lies at approximately -4.9 eV. We add to this the bandgap of amorphous Al_2O_3 with 7 eV [29] and place the conduction band edge at 2.1 eV.

The amount of band bending is directly given by the peak-shift of the Pr $3d$ 5/2 orbital. The BE of the Pr increases after the deposition of Al. The BE increases if the bands are bent downwards, away from the Fermi energy. The magnitude of the band bending is 0.9 eV. This voltage also drops over the AlO_x barrier.

PCMO is a p-type semiconductor with a small bandgap of approx. 0.5 eV [30]. Therefore, we place the Fermi-level in PCMO just above the valence band, and the conduction band 0.5 eV above the valence band.

The XPS measurements show, that the Al/PCMO system has two regions of increased resistance: first the AlO_x barrier and second the space charge region in the PCMO.

In the next section, we are going to approximate the situation with an empirical model of two resistors in series. We will fit this model to electrical transport measurements with the system in different resistive states will be done and we are going to look at the fit parameters of our model and draw conclusions about the ion movement during the SET and RESET process.

B. R(V) curves and the model

We apply triangular voltage sweeps to our devices to get an initial understanding on their electrical response. We measure the resulting resistance and determine the voltages needed to switch the devices.

Figures 3(a) and 3(b) show a representative R(V) measurement for a SC and a PC device, respectively. The SC (PC) device sets for $V < -2V\,(-1.6V)$; both devices reset for $V > 0$, as indicated by the arrows.

Both R(V) curves show one HRS and one LRS branch for $V < 0$. For $V > 0$, the HRS and LRS differ only for the PC sample; the two states do not separate for the SC sample. We will explain this behavior later. The OFF/ON-ratio (R_{HRS}/R_{LRS}) at -1 V is higher for the PC device (OFF/ON-ratio = 64) than for the SC device (OFF/ON-ratio = 2.4).

Here, we want to draw attention to the decay of the LRS of the SC and the PC samples after the switching into a LRS with a slightly higher resistive state than the one that was achieved after one R(V) curve. This decay will be attributed to subloops we will present in Sec. III E.

The slope of the semilogarithmic R(V) curve divides each branch into two parts: the first region (region I, red) with a steep slope, and the second region (region II, yellow) with a shallow slope (Fig. 3). Here, a branch is defined as the R(V) subsection for either LRS or HRS and either $V > 0$ or $V < 0$.

We use an empirical model to investigate the changes in the electrical transport in these two regions while manipulating the state of the device with different electrical biases. Our model only describes the electrical transport for a fixed ion distribution. During SET and RESET, the ion distribution changes. Therefore, the SET and RESET regions are not fitted.

Due to the fact that our devices consist of a combination of two materials in combination we will implement a simple model. The model consists of two resistors R_1 and R_2 in

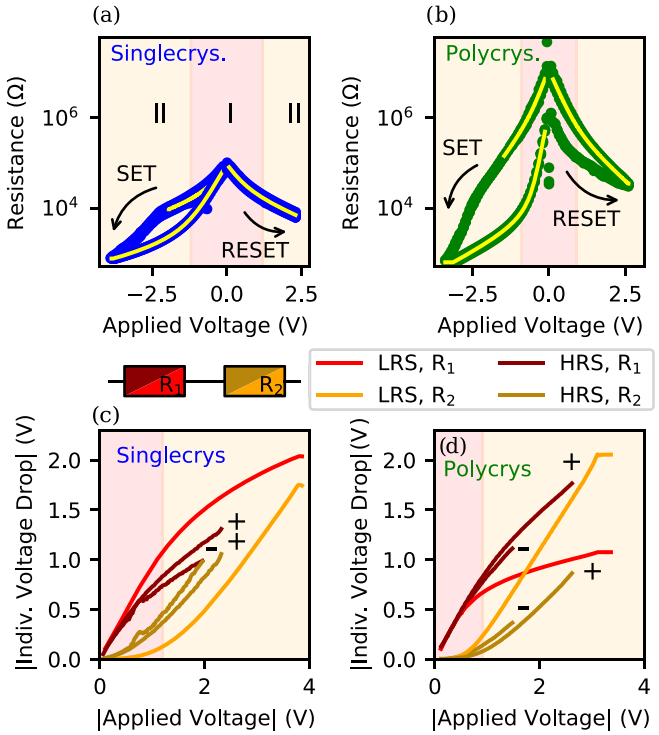

FIG. 3. [(a),(b)] R(V) curves of the measured Al/PCMO system for one SC and one PC device in blue and green, respectively. The yellow curves show the fits of the IV sweep. The area of the measured pads is 2500 μm^2. [(c),(d)] Absolute values of the individual voltage drops over R_1 and R_2 for the SC and PC device, respectively. The branches labeled with + (–) are the different parts of the HRS for the positive and negative voltage branch of the HRS, respectively. The values of the fits can be found in Table I.

series. The formula for their individual resistance is

$$R_{1,2} = \alpha_{1,2} \cdot \exp\left(-V_{1,2} \cdot \beta_{1,2}\right) \tag{1}$$

with $V_{1,2}$ as the individual voltage drop over R_1 and R_2. The sum of V_1 and V_2 is the total applied voltage V. $\alpha_{1,2}$ and $\beta_{1,2}$ are the fit parameters. We are going to relate them to physical parameters in the discussion. Each branch is fitted individually, and the resulting fits describe the data very well [Figs. 3(a) and 3(b), fit in yellow].

Table I shows optimized fitting parameters of the R(V) curves shown in Figs. 3(a) and 3(b).

The fraction $R_1/R_2 = V_1/V_2$ changes with total applied voltage [Figs. 3(c) and 3(d)]. In region I, V_2 is very small and most of the voltage drops over R_1. In region II, there is a higher voltage drop over R_2 and the slope of R(V) decreases. For the SC samples, the voltage drop V_2 is higher in the HRS than in the LRS. Contrary, for PC samples, V_2 is higher in the LRS than in the HRS. This difference is due to different changes in R_1 during the set: in SC samples, α_1 decreases only very little and the changes between the HRS and LRS are dominated by R_2; in PC samples, α_1 decreases much more, which increases V_2.

In summary, both, SC and PC devices SET (RESET) at negative (positive) voltage, however, the PC devices have a much higher OFF/ON-ratio. The current is limited by a non-ohmic transport characteristic, and our empirical model fits the R(V) measurements very accurately.

TABLE I. The fitting parameters for the model described with (1). The left (right) columns belong to the SC (PC) sample. Three different branches have been fitted: the HRS for $V < 0$ before the device sets (HR^-), the HRS for $V > 0$ (HR^+), and the LRS for $V < 0$ (LR^-).

Parameter	HR^+_{SC}	HR^-_{SC}	LR^-_{SC}	HR^+_{PC}	HR^-_{PC}	LR^-_{PC}
$\log_{10}(\alpha_1)$ (Ω)	4.9	4.9	4.9	7.0	7.1	6.2
$\log_{10}(\alpha_2)$ (Ω)	3.8	3.9	2.8	4.8	5.1	3.4
β_1 (V^{-1})	2.4	3.1	2.7	3.5	4.3	8.2
β_2 (V^{-1})	0.8	0.6	0.4	2.1	3.7	0.9

C. The SET process

During the SET process the ion distribution inside the device changes. We study the electronic transport characteristics of different ion distributions by gradually setting the device and monitoring the changes in the R(V) curves. From the changes in the electronic transport we will later draw conclusions about the changes in ion distribution (see Sec. IV C).

The device starts in the HRS after we initialize the virgin device with a voltage sweep of up to 5 V. We cycle the device with the normal switching voltages (SC: −4 V and 2.5 V, PC: −3.8 V and 2.6 V) five times to get a stable R(V) curve. The R(V) curves displayed in Fig. 3 are measured afterwards. The device is reset into the HRS. We investigate the characteristics of the SET process starting from this HRS.

A train of voltage sweeps with increasingly negative voltage and a constant speed of 1 V/s is applied to the device (Fig. S1a, blue sweeps, with in the Supplemental Material [25]). These are the write sweeps, which alter the state of the device. After each write sweep we apply a read-out sweep (red) to the device to check if the write sweep changed the state of the device. The voltage of the read-out sweep is −1.5 V (−1 V) for the SC (PC) samples. We will see that this is the largest negative voltage at which the state of the device does not yet change.

Figures 4(a) and 4(b) show the read-out sweeps of SC and PC samples, respectively. The highest negative voltage of the preceding write sweep is noted in the plot.

From each read-out sweep, the current of the read out sweep is taken and plotted against the SET stop voltage of the preceding write sweep [see Figs. 4(c) and 4(e)]. We define the SET stop voltage as the highest voltages of the preceding write sweep. At −2 V (−1.6 V), the current of the read-out sweep begins to change and the SC (PC) device starts to set (region B, Fig. 4). This confirms, that the voltage of the read-out sweep is indeed too small to alter the state of the device.

The points in grey mark the region where the absolute voltage of the first write sweep is smaller than the absolute voltage of the read-out sweep. We fit our model to each read-out sweep and plot the four parameters again over the SET stop voltage of the preceding write sweep. In region A, all fit parameters are stable and do not change with increasing SET stop voltage.

We subdivide the region where the SET happens further into region B and C. For the SC samples, β_2 increases in region B and decreases in region C. For the PC samples,

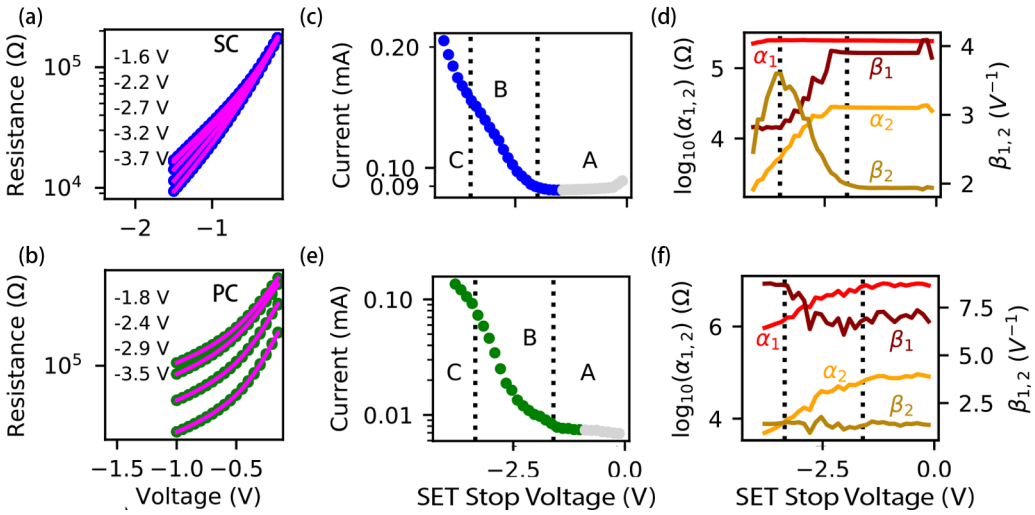

FIG. 4. [(a),(b)] Read-out sweeps belonging to the SC and PC devices, respectively. The SET stop voltage of the preceding write sweep is noted inside each plot. The larger the SET stop voltage of the write sweep, the lower the resistance of the read-out sweep. The corresponding fits are plotted in red.The first and second row present the analysis of the SET process for SC and PC devices, respectively. [(c),(e)] Measured current at the voltage of the read-out sweep vs the SET stop voltage of the preceding write sweep. Each read-out sweep is fitted with our model. [(d),(f)] Parameters of the fit vs the SET stop voltage of the preceding write sweep. The SET process is divided into three regions: Region A where no switching takes places, region B where the switching begins, and region C where the switching intensifies and/or saturates.

β_1 increases in region B and saturates in region C. The transition from region B to C corresponds to a change in slope in Figs. 4(c) and 4(e), respectively.

In summary, both SC and PC devices only set when the applied SET stop voltage is higher than a threshold voltage. This voltage is higher for the SC than for the PC devices ($-2\,\mathrm{V}/-1.6\,\mathrm{V}$). We separate the SET in both SC and PC devices into two regions (B and C). In SC devices, from region B to C the change in current increases, while for PC devices, the change in current decreases.

D. The RESET process

Similar to the SET process, we study the RESET process by gradually resetting the device and monitoring the changes in the electronic transport. From the changes in the electronic transport we draw conclusions about the changes in ion distribution (see Sec. IV C).

From the HRS, a voltage sweep of $-4\,\mathrm{V}(-3.8\,\mathrm{V})$ switches the SC (PC) device into the LRS. Directly afterwards, we investigate the voltage dependence of the RESET process by again using a combination of write sweeps with increasing RESET stop voltage and constant read-out sweeps. The RESET stop voltage is defined analog to the lines of the SET stop voltage as highest voltage of the RESET sweep. The sweep speed of all sweeps is $1\,\mathrm{V/s}$.

The RESET stop voltage (Fig S1b, blue sweep, within the Supplemental Material [25]) starts at 0.1 V, increases, and stops at 5 V. This is much higher than the normal RESET voltage of 2.5 V (2.6 V) for the SC (PC) samples. We increased the RESET stop voltage to see, if we can activate different regimes of ionic motion at higher voltages.

A read-out sweep (Fig S1b, red sweep, within the Supplemental Material [25]) follows each write sweep. All read-out sweeps have a constant stop voltage of $-1.5\,\mathrm{V}$ ($-1.2\,\mathrm{V}$) for the SC (PC) samples.

Figures 5(a) and 5(b) show the measured read-out sweeps for the SC and PC samples, respectively. The RESET stop voltage of the preceding write sweep is noted inside the plot. As the RESET stop voltage increases, the resistance of the read-out sweep increases. The fit to each read-out sweep is shown in magenta.

Figures 5(c) and 5(e) show the current at the voltage of the read-out sweeps versus the RESET stop voltage of the preceding write sweep for SC and PC samples, respectively. Each point belongs to one read-out sweep. It is important to note that the reset starts for both SC and PC devices already with stop voltage of $V = 0.1\mathrm{V}$.

We fitted each read-out sweep with our model. Figures 5(d) and 5(f) show the optimized fit parameters versus the RESET stop voltage of the preceding write sweep.

Similar to the SET process, we divide the RESET process into three different regions A, B, and C. Their distinction is best visible for the SC sample [Fig. 5(c)]. In region A, the RESET process begins. In region B, the RESET process slows down. In region C, the strength of the RESET process increases again. Going from A to C, the fit parameters α_2 and β_2 change the most: α_1 increases strongly, saturates, and then increases gradually; β_1 decreases strongly, saturates and then increases gradually, too.

For the PC device, the current during the RESET does not show regions with different slopes. We identify the regions based on the behavior of the fit parameters. From region A to B, β_2 saturates; from region B to C, α_1 and α_2 saturate.

In summary, the RESET already starts for both SC and PC devices at $V = 0.1\mathrm{V}$. We attribute these low switching voltages to the presence of an internal field caused by the charge region that additionally accelerates the oxygen vacancies into the PCMO layer.

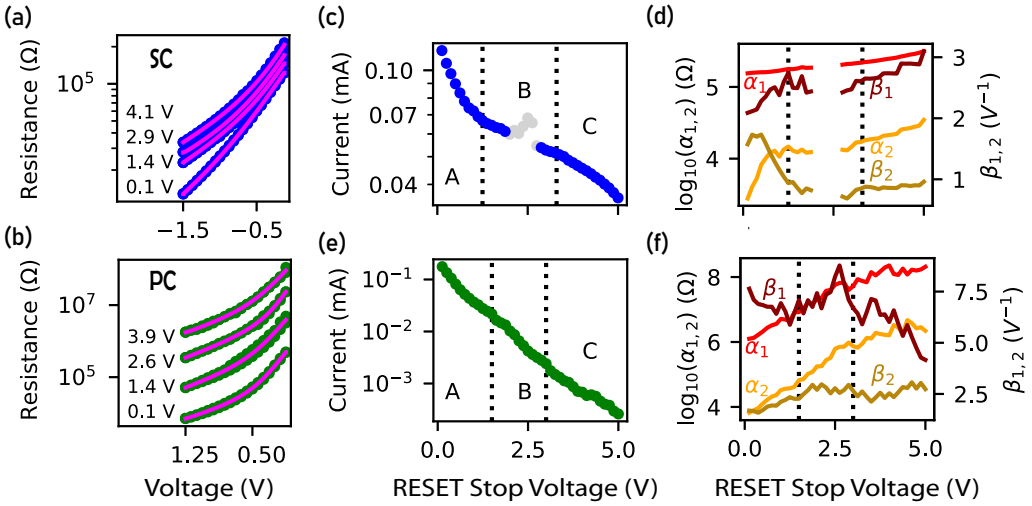

FIG. 5. [(a),(b)] Read-out sweeps of the SC and PC samples, respectively. The RESET stop voltage of the preceding write pulse is noted inside each plot. The fits are shown in red. [(c),(e)] Current of the read-out sweep vs the RESET stop voltage of the preceding write sweep for the SC and PC device, respectively. Each point belongs to one read-out sweep. [(d),(f)] The optimized fit parameters vs the RESET stop voltage of the write sweep for the SC and PC device, respectively.

We split the RESET process into three different regions. For the SC devices, the three regions are very easily distinguishable, with a slowing of the RESET process in region B. At very high voltages, the resistance change saturates (region C). In contrast, the PC devices RESET much more homogeneously exhibiting a more or less linear curve in Fig. 5(e).

E. Subloops

We looked at the changes in the electronic transport with changes in the ion distribution. In this section, we investigate transient changes in the electronic transport, which are, as we will explain later, not associated with the movement of ions but to the charging of traps inside the AlO_x barrier (see Sec. IV D).

In the LRS, a negative voltage sweep can excite a volatile LRS with an even lower resistance than the nonvolatile LRS. When sweeping the voltage ($0\,\mathrm{V} \rightarrow -V$), the resistance is higher than the resistance of the back sweep ($-V \rightarrow 0\,\mathrm{V}$), resulting in a small hysteresis. We call this observation subloops. Figure 6 shows the subloop measurements on the SC and PC samples. The subloop state decays exponentially within a few ms into a LRS with a slightly higher resistance, as can be seen in Fig. S3 within the Supplement Material [25]. Based on this fast time scale of decay, we conclude that these states are not related to a redistribution of ions but to a relaxation of electrons from traps [31,32].

We prepare our devices in the HRS. A voltage sweep with the standard SET voltages sets the device into the LRS. A second sweep with the same voltage excites the volatile LRS and a small hysteresis between the up and down sweep is visible. Repeating the same voltage sweep again reproduces the same hysteresis, showing that the additional decrease in resistance is volatile.

We investigate the subloops regarding the voltage that is needed to excite the volatile LRS and the changes in the fitting parameters between the volatile and nonvolatile LRS. Starting with the normal SET voltages, we apply voltage sweeps with decreasing SET stop voltage and record the resulting R(V) curves. Figures 6(a) and 6(c) show a small subset of all collected R(V) curves as examples of the measured subloops in the SC and PC samples, respectively.

The right y axes of Figs. 6(a) and 6(c) show the calculated hysteresis area A_{Hyst}. The lower border of the y axis equals $A_{\mathrm{Hyst}} = 0$. The used formula is

$$A_{\mathrm{Hyst}} = \frac{1}{|V|}\left(\int_V^0 R_{nv}(V)dV - \int_V^0 R_v(V)dV\right) \qquad (2)$$

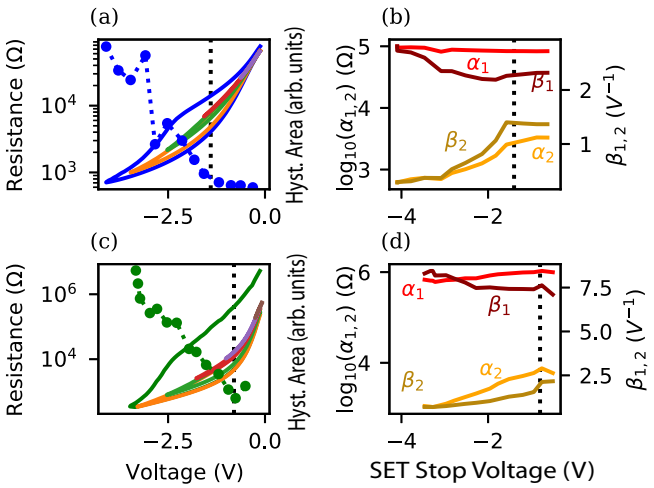

FIG. 6. [(a),(c)] R(V) curves of the SC and PC samples, respectively. The device starts in the HRS and a voltage sweep sets the device into the LRS. The SET stop voltage of subsequent sweeps is decreased. The right axes shows the opening of the subloop vs the SET stop voltage. [(b),(d)] The evolution of the fitting parameters over the applied voltage for the SC and PC samples, respectively.

with A_{Hyst} being the area of the hysteresis, V the voltage of the sweep, $R_{nv}(V)$ the nonvolatile part of the R(V) sweep, and $R_v(V)$ the volatile part of the R(V) sweep.

Figures 6(b) and 6(d) show the evolution of the fitting parameters with decreasing SET stop voltage for the SC and PC samples, respectively. The qualitative change is very similar between the SC and the PC sample. For small voltages, the area of the hysteresis is close to zero and all the fit parameters stay the same. The nonvolatile LRS is not yet excited. When the SET stop voltage of the applied sweep is higher than -1.4 V (-0.8 V) for the SC (PC) samples, the hysteresis area increases. Equally, the fit parameters are changing: α_1 stays constant, β_1 increases, α_2 and β_2 decrease. The magnitude of the change is higher for the PC samples.

In summary, both SC and PC devices show a volatile decrease in resistance in the LRS that decays on the ms time regime. For SC (PC) devices, the volatile state is excited for $V < -1.4$ V(-0.8 V). The decrease in resistance is higher the higher the SET stop voltage is.

F. Impedance spectroscopy

To verify our model with two resistors in series and to gain knowledge about their possible physical origin, we perform impedance spectroscopy (IS) on the HRS of the SC samples. We also measured PC samples. However, their much higher resistance at smaller absolute voltages produced much smaller currents, which lead to very noisy IS measurements. We therefore restrict ourselves to the data of the PC samples

We chose to measure the HRS of the SC samples because the voltage drop is rather evenly distributed between the two resistors and the HRS is more stable because no subloops occur in the HRS.

Figure 7(a) shows the normalized Nyquist plots, measured at different applied dc voltages. For each applied dc voltage, the complex impedance was normalized with the impedance at 2×10^3 Hz. Figure 7(b) shows the real part of the values used for the normalization. The imaginary part is negligible.

The frequency range spans from 2×10^3 Hz to 3×10^5 Hz. We fit the impedance data using the python package `impedance.py` [33]. The equivalent circuit used in the fitting consists of two parallel capacitor-resistor pairs in series with each other. This resembles the circuit of our own model with two added capacitors. The four fitting parameters are C_1, R_1^{IS}, C_2, and R_2^{IS}. This equivalent circuit fits the data very well. Using only one R-C pair to describe the data lowers the accuracy of the fit visibly (see Fig. S2 within the Supplemental Material [25]). Previous measurements with two very visible semicircles support the equivalent circuit of two R-C pairs [34].

Figures 7(c) and 7(d) show the evolution of the four fitting parameters with the applied dc voltage. Both resistors decrease with applied voltage and $R_1^{IS} > R_2^{IS}$, as expected in the two resistor model for R_1 and R_2.

The capacitance contribution to the impedance is dominated by a much smaller C_1. C_1 decreases with voltage with a change in slope at -0.5 V. C_2 is increasing exponentially by one order of magnitude from 1 nF to 10 nF. For voltages smaller than -0.8 V the increase starts to saturate.

In summary, we see that a model of two R-C parts in series describes the IS measurements very well. The extracted values for the resistance fit to the expected values of R_1 and R_2 based on the values of Sec. III B. The two capacitance values are very different ($C_1 \ll C_2$) and with applied voltage C_1 decreases and C_2 increases.

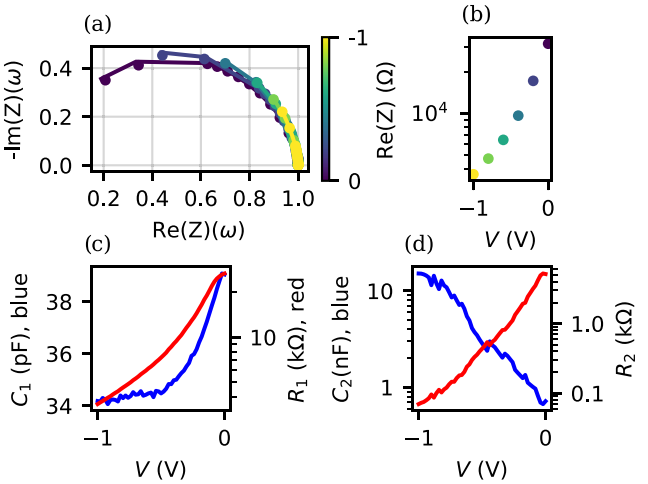

FIG. 7. (a) Nyquist plot of the HRS of the SC samples. The frequency ranges from 2×10^3 Hz to 3×10^5 Hz. The color represents the applied dc voltage from 0 V to -1 V. For better visibility, the Nyquist-data for each dc voltage is normalized to the z value at 2×10^3 Hz. The values of the applied dc voltages shown here is only a small subset of all applied dc voltages. (b) The real value of Z at 2×10^3 Hz at different applied dc voltages. These values are used to normalize the data in (a). (c) The capacity and resistance of the first R-C-parallel circuit as a function of applied dc voltage. (d) The capacity and resistance of the second R-C-parallel circuit as a function of applied dc voltage.

IV. DISCUSSION

A. Physical origin of R_1 and R_2

In this section we identify the origin of R_1 and R_2 by considering the electrical, XPS, and IS measurements.

First, Fig. 3 shows that the current is limited by a non-ohmic current transport. Therefore, we exclude all ohmic junctions, including the PCMO/Pt and PCMO/SRO junctions, which have an ohmic characteristic, too [24]. The remaining system of interest consists of the Al/PCMO stack.

Second, we consider the outcome of the XPS measurements (Fig. 2). As already stated in Sec. III A, the changes in the Al $2p$ and Mn $2p$ orbitals indicate the formation of an interface layer between the Al and PCMO. Oxygen ions from the PCMO move into the Al and oxidize it at the interface. They leave behind an oxygen deficient region in the PCMO. Additionally, the position of the Pr peak changes after the deposition of Al. As already discussed in Sec. III A, this indicates a downward band bending at the interface between the PCMO and the Al. The band bending forms a depletion or even inversion layer with increased resistance in the PCMO.

In summary, the XPS measurements reveal two regions with increased resistance at the interface: On the Al side the formation of an insulating AlO_x layer, and on the PCMO side the formation of a hole depletion zone and a region of oxygen deficient PCMO. We expect the high-bandgap AlO_x layer to

have a much higher resistance than the depletion layer of the small bandgap semiconductor PCMO. Since $R_1 > R_2$ we identify R_1 with the AlO_x layer and R_2 with the oxygen deficient PCMO and its hole depletion layer.

For further confirmation, we consider the IS measurements (Fig. 7). First, the measurements match very well with a model of two C-R parallel circuits in series. This supports our assumption that there are only two regions, that dominate the resistance of the whole system. The fitting of the IS measurements also returns values for the two resistors R_1 and R_2: R_1 and R_2 are approximately exponentially decreasing with applied voltage and $R_1 > R_2$, as expected.

Next, we look at the expected values of the capacitance. We use the formula for a parallel plate capacitor to calculate the capacitance of the AlO_x layer,

$$C = \epsilon \cdot \epsilon_r \frac{A}{d}, \tag{3}$$

with $A = 2500\,\mu m^2$ as the device size, $\epsilon_r = 7$, and $d = 4\,nm$ as the thickness of the interfacial AlO_x layer. The expected capacitance at 0 V is $C_1 \approx 39\,pF$. With an applied negative voltage, the current flows through excited, shallow traps [35–37]. While uncharged defects increase the capacitance, ionized defects lower the capacitance [38]. Therefore, we expect C_1 to start at 39 pF and decrease with increasing, absolute applied voltage. This behavior is observed during the IS [see Fig. 7(c)].

We calculate the capacitance of the hole depletion layer in the PCMO again with Eq. (3), but with $\epsilon_r = 110$ [39]. We expect a very small depletion layer of $d \approx 2\,nm$, since the PCMO has a lot of free charges with a doping level of 30% to screen the internal voltage drop. The expected capacitance at 0 V is $C_2 \approx 1\,nF$. A negative voltage neutralizes the depletion layer, and we expect C_2 to increase. Again, this exactly is the observed behavior in our IS measurement.

In summary, we have identified the two regions where it is most likely that the most voltage drops: the AlO_x barrier and the oxygen depleted PCMO with the hole depletion region. We looked at the expected resistance and capacitance values and identified R_1 as the AlO_x barrier and R_2 as the oxygen deficient and hole depleted layer in the PCMO.

B. Identification of fit parameters

After identifying R_1 and R_2 with the AlO_x and PCMO, respectively, we are now going to discuss the physical meaning of the fit parameters α_1, α_2, β_1, and β_2. We are going to look at analytic current-voltage expressions for the AlO_x and PCMO and compare their parameters to our model.

We expect our AlO_x barrier to be amorphous and full of shallow defects, which the applied voltage ionizes. The electrons released to the conduction band contribute to the current. Frenkel derived a very simple, analytic formula describing this situation [40]. This formula describes the ionization of a single electron from a trap with a $\frac{1}{r}$ potential into the conduction band. The process is called the Poole-Frenkel effect and describes the resistance with

$$R \propto \exp\left(\frac{e}{k_B T}(\phi_B - 2\sqrt{eV/(4\pi\epsilon d)})\right) \tag{4}$$

with V as the voltage drop over the AlO_x barrier, e as the elementary charge, k_B as the Boltzmann-constant, T as the temperature, ϵ as the permittivity of the barrier, d as the thickness of the barrier, and ϕ_B as the barrier height at zero applied electric field.

If we now compare the two resistor model to the different transport mechanisms, keeping in mind the screening of the barrier, we can approximate that

$$\beta_1 \propto \frac{1}{\sqrt{\epsilon d_s}}. \tag{5}$$

We exchange d with d_s to stress that screening changes the barrier width with the permittivity of the material [41]. For decreasing ϵ, d_s decreases as well. ϵ changes with a high, local concentration of $V_O^{\bullet\bullet}$.

To identify α_1, we assume that each ionized trap adds one free charge carrier. For homogeneously distributed traps it then follows that

$$\alpha_1 \propto \frac{1}{n_t}, \tag{6}$$

with n_t as the total number of traps in the barrier.

In PCMO, described by α_2 and β_2, polarons carry the electric current [24,42]. The resulting resistance is described by

$$R \propto \frac{V}{n_p e a \omega} \frac{1}{\sinh(x(V))} \exp\left(\frac{\Delta W_{ac}}{k_B T}\right) \tag{7}$$

with

$$x(V) = \frac{eVa}{2k_B T r}, \tag{8}$$

and V as the applied voltage, n_p the polaron density, e the elementary charge, a the hopping distance, ω the hopping frequency, ΔW_{ac} the activation energy for hopping, k_B the Boltzmann constant, T the temperature, and r the thickness of the hopping region. In our case, the thickness r is equal to the thickness of the depletion zone, because V_2 mostly drops over the insulating depletion layer and not over the rest of the highly doped PCMO. The hopping distance a is 0.4 nm, the distance between two neighboring Mn ions [24].

For $|x(V)| > 1$, $2 \cdot \exp(-x(V))$ approximates $1/\sinh(x(V))$ very well. We compare the exponent $x(V)$ to the exponent of our model (1) and find that

$$\beta_2 \propto \frac{1}{r}. \tag{9}$$

Pithan *et al.* [43] showed that with decreasing oxygen content, the mobility μ of the charge carrier drops by one order of magnitude, and the charge carrier concentration n drops by 10%. Therefore

$$\alpha_2 \propto \frac{1}{\mu n_p}. \tag{10}$$

A lower concentration of charge carriers n_p lowers the screening of the internal field and increases the width r of the depletion layer. We therefore expand Eq. (9) to

$$\beta_2 \propto n_p. \tag{11}$$

In summary, we compare our model equations to the equations for Polaron hopping (7) in the PCMO and Poole-Frenkel transport (4) in the AlO_x. This comparison connects our

TABLE II. A summary of the Fit parameters, their connection to physical parameters, and the interpretation of this connection.

Fit param.	Prop. to	Interpretation
α_1	$1/n_t$	Base resistivity of the whole AlO_x barrier.
β_1	$1/(\sqrt{\epsilon d_s})$	Modification of the E field by screening.
α_2	$1/(\mu n_p)$	Base resistivity of PCMO: The amount of charge carriers and their mobility.
β_2	$1/r$, n_p	Modulation of the E field in the depletion zone by its width.

fitting parameters to physical parameters (Table II) and the $V_O^{\bullet\bullet}$ distribution.

C. Ion movement

As stated in Sec. I, there exists a general agreement that switching in VCM based devices is attributed to the movement of oxygen vacancies. For our system, we expect the following general trend: In AlO_x, additional oxygen vacancies act as defects and traps and increase the leakage current, i.e., decrease the resistance. In PCMO, additional oxygen vacancies predominantly break the oxygen chains between the Mn ions [43] and partly neutralize the hole doping by electronic charge compensation. As a result of both, the resistance increases. Therefore, we expect the SET and RESET for $V < 0$ and $V > 0$, respectively: A negative bias pushes the positively charged oxygen vacancies into the AlO_x and a positive bias pushes them back into the PCMO. We observe this behavior for SC and PC devices. Therefore, the observed switching polarity in our devices is consistent with the reversible movement of oxygen vacancies between the AlO_x and the PCMO layer.

Although the SET and RESET have a similar mechanism in SC and PC devices, Figs. 4(d) and 4(f) (SET fitting parameters), and Figs. 5(d) and 5(f) (RESET fitting parameters) show two systematic differences between the SC and PC devices. First the base resistivity of the AlO_x (α_1) starts to change at different voltages for the two types of devices. This means, that during the SET in SC devices, the amount of traps inside the AlO_x barrier only changes at very high voltages although α_2 changes already at lower voltages. In contrast, for the PC devices α_1 starts changing as soon as α_2 starts changing. However, during the RESET, its changes for both devices for the lowest voltage $V = 0.1V$. Second, the trend of the modification of the E field by screening (β_1) is opposite: When SC devices set (reset), β_1 generally decreases (increases). When PC devices set (reset), β_1 generally increase (decrease).

One point that might explain the different behavior of α_1 is the difference in voltage drop over the different layers. In particular, the difference in V_1/V_2 between the PC and SC HR^+ might explain the differences in the behavior of the resistivity of the AlO_x (α_1) during the SET. Since $V_1(\mathrm{PC}) > V_1(\mathrm{SC})$, the PC device reaches the threshold voltage needed for moving oxygen vacancies inside the AlO_x much earlier. Different microscopic reasons can cause this difference in the resistances between the SC and the PC samples, namely, the thickness of the AlO_x layer, the oxidation state of the AlO_x and the crystallinity of the PCMO layer. The latter two effects could cause a different mobility for the oxygen vacancy drift and diffusion [44].

The threshold voltage for oxygen vacancy movement depends on the activation energy for the diffusion, modified by the internal voltage drop at the space charge region. The internal voltage of 0.9 V drops over the AlO_x barrier, with the negatively charged depletion layer in the PCMO as the anode [see Fig. 2(d)]. This internal voltage pushes the oxygen vacancies towards the PCMO, facilitates the RESET and hinders the SET. Additionally, oxygen vacancies at the interface gain energy by entering the PCMO [34]. These two effects could explain the different voltage behavior of the amount of trap states inside the AlO_x during SET and RESET as well as the resulting resistivity of the barrier (α_1) and the different starting voltages.

Now, we move on to the differing behavior of the modification of the E field by screening (β_1) between the SC and PC devices. Equation (5) connects β_1 to the permittivity of the barrier. As stated earlier, the permittivity increases with uncharged traps and decreases with charged traps. We postulate, that with the applied read-out voltage, the majority of the traps is uncharged in SC devices, decreasing β_1. In PC devices, the voltage is sufficient to ionize the traps, and β_1 increases. Two observations support our claim: First, XPS measurements of the VB show, that the VB of the AlO_x on the PC devices is 0.6 eV lower than the VB of the AlO_x on SC PCMO (Fig. S5 within the Supplemental Material [25]). This places the traps at a lower energy with respect to the conduction band and makes them easier to ionize. Second, the subloops start appearing in PC samples at lower absolute voltage. We will see later that the subloops are also connected to the charging of traps. Their earlier appearance supports our claim, that we need smaller energies to excite the traps in the PC than in the SC devices.

In summary, the movement of oxygen vacancies explains the switching direction of the observed resistance change. The different defect configuration in the AlO_x explains the differences in modification of the E field by screening (β_1). With respect to resulting resistivity of the barrier (α_1), various microstructural reasons can cause the differences in the behavior for the SC and PC samples.

In the following we are going to explicitly state when and where the oxygen vacancies move. This movement is going to explain the changes in the fit parameters during SET and RESET.

1. SET

In this section, we explain the movement of oxygen vacancies during the SET and the observed changes in the fit parameters.

Figure 8 shows schematically the distribution of oxygen vacancies in the AlO_x and the SC and PC PCMO in the HRS and during the SET process. The different subplots correspond to the regions A, B, and C in Figs. 4(c) and 4(e). The dashed

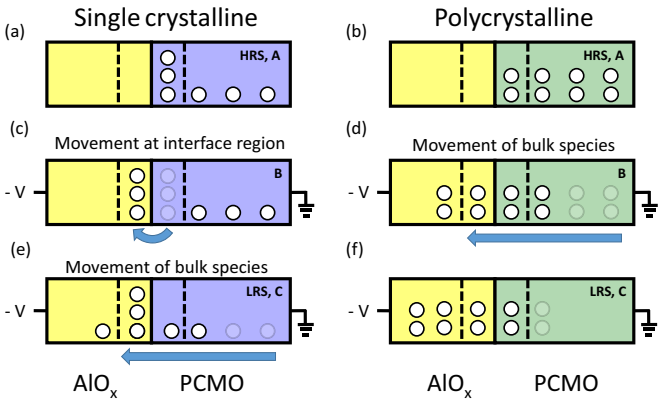

FIG. 8. The movement of oxygen vacancies during the SET. The left and right column depict the movement in the SC and PC devices, respectively. The different plots correspond to the regions A, B, and C for the SC or PC SET process in Figs. 4(c) or 4(e), respectively. The yellow block is AlO_x, the purple block SC PCMO and the green block PC PCMO. The white circles stand for the oxygen vacancies. The dashed lines mark the interface region in each material. The blue arrows indicate the movement of the oxygen vacancies in and between the different regions. Additionally, the applied voltage during the SET is indicated.

lines mark the "interface region": one unit cell on the side of the AlO_x and PCMO, respectively.

Figure 8(a) depicts the HRS in the SC devices and corresponds to Fig. 4(c), region A. The oxygen vacancies are located in the PCMO. Inside the PCMO, the oxygen vacancies accumulate near the interface, because the transport inside the SC PCMO needs a high activation energy.

Figure 8(c) depicts the initial set process and corresponds to Fig. 4(c), region B. The voltage shifts the oxygen vacancies at the interface into the AlO_x. They do not move further because $|V_1|$ is not large enough to enable oxygen vacancy-movement inside the barrier, at this voltage (see Sec. IV C). Also $|V_2|$ is not yet high enough to enable transport inside the SC PCMO.

The oxygen vacancies in the interface region of the AlO_x introduce a large number of traps locally. Their inherent dipole increases ϵ and d_s. In turn, the modification of the electric field by screening (β_1) decreases. The trap free remainder of the barrier still limits the Poole-Frenkel current, leaving the amount of traps in the barrier unchanged (α_1).

The interface region in the PCMO is now fully oxidized. In turn the mobility μ increases, and is now limited by the bulk part of the PCMO film that still contains oxygen vacancies: The base resistivity of the PCMO decreases (α_2). The increase in free charge carriers n_p also increases the modulation of the electric field in the depletion zone (β_2). Figure 8(e) depicts the final state of the set process and corresponds to Fig. 4(c), region C. The high applied $|V|$ enables the bulk transport of oxygen vacancies inside the PCMO and AlO_x. Oxygen vacancies from the bulk PCMO move to the fully oxidized interface region in the PCMO. Moreover, oxygen vacancies move to the AlO_x barrier and the resistance of the barrier decreases (α_1). $|V_1|$ increases as the voltage drop over the PCMO decreases. $|V_1|$ is now high enough to ionize the first traps in the barrier. The contribution from excited and not excited traps cancel each other out, and the modulation of the E field in the depletion zone stays constant (β_2). The total amount of oxygen vacancies in the PCMO decreases, and so does the resistivity of the PCMO (α_2). However, the increased concentration of oxygen vacancies at the interface lowers n_p and decrease the modulation of the E field of the depletion zone (β_2). Figure 8(b) shows the HRS in the PC samples and corresponds to Fig. 4(e), region A. All oxygen vacancies that participate in the switching mechanims are localized in the PCMO. Figure 8(d) shows the beginning of the set and corresponds to Fig. 4(e), region B. Oxygen vacancies are moving from the PCMO into the AlO_x. Extended defects in the PC PCMO facilitate the transport inside the PCMO and a high R_1 and $|V_1|$ activate the transport inside the AlO_x. The increase of oxygen vacancies in the AlO_x bulk decreases the resistivity of the whole AlO_x barrier (α_1). The high $|V_1|$ ionizes the new traps and ϵ decreases; β_1 increases. The region with high oxygen vacancies concentration and low mobility μ gets shorter and the conductivity of the PCMO decreases (α_2).

Figure 8(f) shows the saturation of the SET and corresponds to Fig. 4(e), region C. Almost all oxygen vacancies have been transported to the interface or inside the AlO_x. The oxygen vacancy-concentration in the AlO_x (PCMO) further increases and resistivity of the AlO_x/α_1 continues to decrease. Additionally, the oxygen vacancy-concentration in the PCMO further decreases and the resistivity of the PCMO decreases (α_2). The AlO_x becomes very conductive and $|V_1|$ decreases accordingly. $|V_1|$ is not sufficient to ionize traps deep inside the AlO_x. These uncharged traps cancel the effect of the charged traps and the modification of the E field by screening (β_1) stays constant.

During the whole SET process, the concentration of oxygen vacancies in the PCMO interface region stays constant. Therefore, the modulation of the E field in the depletion zone by its width (β_2) also stays constant.

2. RESET

Figure 9 schematically shows the distribution of oxygen vacancies in the AlO_x and the PCMO in the LRS and during the RESET process. The different subplots correspond to the LRS, and regions A, B, and C in Figs. 5(c) and 5(e). The dashed lines mark the "interface region", i.e., one unit cell on the side of the AlO_x and PCMO, respectively.

Figures 9(a) and 9(b) are the same plots as Figs. 8(e) and 8(f), respectively and are only shown here for completeness.

Figure 9(c) shows the beginning of the RESET in the SC samples and corresponds to region A in Fig. 5(c). The oxygen vacancies move from the AlO_x interface region into the PCMO interface region. The internal voltage and difference in Gibbs free energy facilitate this process (see Sec. IV C).

The loss of oxygen vacancies increases the resistivity of the AlO_x barrier(α_1) and increases the modification of the E field by the screening (β_1). However, the increases of the resistivity of the AlO_x barrier (α_1) is small, because the main change in oxygen vacancy concentration happens at the interface and not within the barrier.

The increasing interfacial oxygen vacancy concentration in PCMO increases its resistivity (α_2) and decreases the modulation of the E field in the depletion zone (β_2).

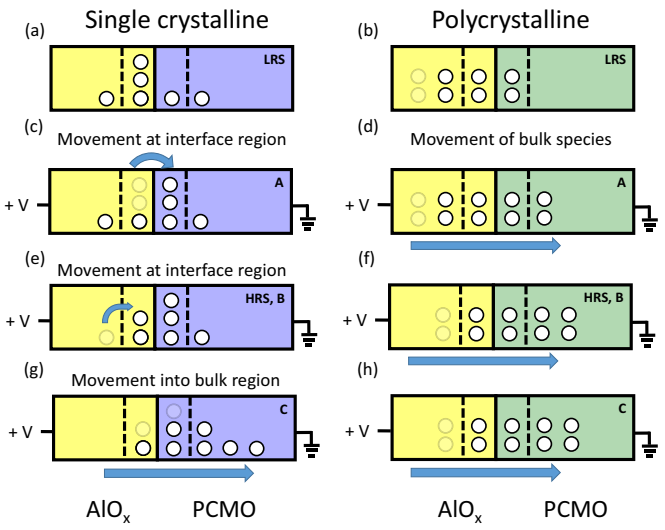

FIG. 9. The movement of oxygen vacancies during the RESET. The left and right column depict the movement in the SC and PC devices, respectively. The different plots correspond to the LRS and regions A, B, and C for the SC or PC RESET process in Figs. 5(c) or 5(e), respectively. The yellow block is AlO_x, the purple block SC PCMO and the green block PC PCMO. The white circles represent the oxygen vacancies. The dashed lines mark the interface region in each material. The blue arrows indicate the movement of the oxygen vacancies in and between the different regions. Additionally, the applied voltage during the RESET is indicated.

Figure 9(e) shows the RESET, after the initial interface transport has saturated, and it corresponds to region B in Fig. 5(c). The PCMO interface contains a high concentration of oxygen vacancies and the transport inside the SC PCMO is not yet activated. Only the oxygen vacancies inside the AlO_x move closer to the interface.

This redistribution ruptures the trap conduction path inside the AlO_x and increases its resistivity (α_1). The overall concentration of oxygen vacancies stays constant and so does the modification of the E field (β_1). On the other hand, the oxygen vacancy distribution in the PCMO does not change.

At this voltage, the normal RESET voltage is reached, and the device has gone through a complete cycle of HRS → LRS → HRS. The HRS after one cycle [Fig. 9(e)] has a higher concentration of oxygen vacancies in the AlO_x than the initial HRS [Fig. 8(a)]. Consequently, the HRS after one cycle has a lower resistance than the initial HRS. This is also observed in experiment, where the resistance of the HRS decreases with the number of cycles (Fig. S6 within the Supplemental Material [25]).

Figure 9(g) shows the RESET at very high $|V|$, and it corresponds to region C in Fig. 5(c). The applied voltage $|V|$ is higher than for a normal RESET. Now, the oxygen vacancy transport inside the PCMO is activated and all the residual oxygen vacancies move deep into the PCMO. The loss of oxygen vacancies increases the resistivity of the barrier and the modification of the E field (α_1/β_1). The additional oxygen vacancies in the bulk PCMO increase its resistivity (α_2). Oxygen vacancies at the interface of the PCMO move deeper inside the PCMO, release n_p, and increase the modification of the E field in the depletion zone (β_2).

Figure 9(d) shows the beginning of the RESET for the PC samples and corresponds to Fig. 5(f), region A. Oxygen vacancies move from the AlO_x over the interface into the PCMO. The noninterfacial AlO_x loses oxygen vacancies and the amount of traps in the barrier decreases (α_1 increases).The additional oxygen vacancies inside the PCMO increase its resistivity (α_2). We attribute the decrease in modification of the E field by screening (β_1) and increase in the modulation of the E field in the depletion zone (β_2) to a measurement artefact. We used a read-out voltage of -1.2 V. As presented in Sec. III E, -0.8 V is already sufficient to excite the volatile LRS in which increases β_1 and decreases β_2. During RESET, the volatile state vanishes and β_1 (β_2) decreases (increases). Therefore, we attribute the changes in $\beta_{1,2}$ that we see in Fig. 5(f), region A to the vanishing subloops, not to changes in the ionic configuration.

Figure 9(f) shows the continuation of the RESET and corresponds to Fig. 5(f), region B. More oxygen vacancies move from the AlO_x into the PCMO. Only the interfacial AlO_x still contains some oxygen vacancies. The continued movement of the oxygen vacancies increases the resistivity of the barrier and the PCMO (α_1/α_2). Two effects change β_1: First, V_1 increases from the LRS to the HRS. A higher voltage drop increases the number of ionized traps, decreases ϵ and increases β_1. This effect dominates for the first half of region B. Second, the number of (ionized) oxygen vacancies in the AlO_x decreases, which increases ϵ and decreases β_1. This effect dominates for the second half of region B. The oxygen vacancies concentration stays constant in the depletion zone, and therefore β_2 stays constant as well.

Figure 9(h) shows the RESET at very high $|V|$ and corresponds to Fig. 5(f), region C. The interfacial oxygen vacancies in the AlO_x move into the PCMO. The noninterfacial oxygen vacancies in the AlO_x and PCMO have already reached their final values and the resistivity of the AlO_x and the PCMO (α_1 and α_2) saturates. The oxygen vacancy concentration stays constant in the depletion zone, and β_2 stays constant as well. The loss of oxygen vacancies in the AlO_x interface layer continues the decrease of ionizable traps, and the decrease of β_1.

In summary, the movement of oxygen vacancies explains the changes in the fit parameters seen during the SET and RESET process. The difference in oxygen vacancy mobility in the PCMO and the resulting changes in V_1/V_2 explain the differences between SC and PC samples due to their different microstructure. The polarity of the built-in voltage and the high oxygen affinity of Al explain the asymmetry between SET and RESET.

D. Origin of the subloops

In this section, we move from the impact of the ionic movement to the impact of electronic contributions to the observed resistance changes. As discussed in Sec. III E, a high negative $|V|$ can excite a volatile resistance decrease, namely subloops, in the LRS. We are going to explain the volatile state by looking at trap states deep inside the AlO_x band gap.

Figure 6 shows measurements, which reveal a volatile LRS. An applied voltage ($V_{SC} = -1.4$ V, $V_{PC} = -0.8$ V) excites the change in resistance: The higher $|V|$, the lower the resistance. La Torre *et al.* [45] observed subloops in the HRS,

originating from a volatile state in Ta_2O_5 devices. They attribute the change in resistance to a charging of trap states. No details of the position and origin of the traps are given. In contrast, we observe the subloops in the LRS, but we also suggest to attribute this change in resistance to a charging of trap states.

Please note that we assume to have two types of traps in the AlO_x. The traps connected to the Poole-Frenkel transport in the barrier are shallow traps, lying very close to the conduction or valence band. The traps connected to the subloops are traps deep inside the band gap of the AlO_x barrier. Furthermore, we assume that we still have a highly oxidized barrier at the interface between the PCMO and the Al even in the LRS. This can be concluded from the explanation of the SET process given in Sec. IV C 1. The degree of oxidation of the Al decreases with the distance to the PCMO interface.

We therefore conclude that we build AlO_x with unknown oxygen content with a high density of trap states deep inside the band gap.

Figure 10 shows the band structure of a SC sample in the LRS at different applied voltages; (c), (d), and (e) show the voltages $-1.4\,\mathrm{V}$, $-4.1\,\mathrm{V}$, and $-1.4\,\mathrm{V}$, respectively. $-1.4\,\mathrm{V}$ in the down sweep is the threshold to ionize the traps. In contrast, the traps are still ionized at $-1.4\,\mathrm{V}$ during the up sweep. We calculate the individual voltage drop V_1 and V_2 with the parameters given in Fig. 6(d). For Fig. 10(a), we use $\log_{10}(\alpha_1) = 5.0\,\Omega$, $\beta_1 = 2.3\,\mathrm{V}^{-1}$, $\log_{10}(\alpha_2) = 3.4\,\Omega$, and $\beta_2 = 1.4\,\mathrm{V}^{-1}$. This corresponds to no excitation of the volatile state. For Figs. 10(b) and 10(c), we use $\log_{10}(\alpha_1) = 5.0\,\Omega$, $\beta_1 = 2.7\,\mathrm{V}^{-1}$, $\log_{10}(\alpha_2) = 2.8\,\Omega$, and $\beta_2 = 0.3\,\mathrm{V}^{-1}$. This corresponds to an excitation of the volatile state with $V_{\mathrm{max}} = -4.1\,\mathrm{V}$.

V_1 starts to ionize the traps when the Fermi level in the Al and the traps align since this enables electrons to tunnel into the traps and charge them. Therefore, we place the trap level at 1.8 eV below the CB [Fig. 10(a)]. This agrees with simulations and experiments of traps in amorphous AlO_x [46,47].

At -4.1 eV, all traps are ionized [Fig. 10(b)]. The differences between (a) and (b) explain the parameter changes in Figs. 6(b) and 6(d).

The ionized traps generate an electric potential, which deforms the potential landscape compared to the case without ionized traps (blue area). The trap potential moves the traps upwards, until they are fixed at the threshold voltage for their ionization. The trap potential also reaches into the PCMO, and bends the bands upwards. This partially neutralizes the depletion zone and the resistivity of the PCMO (α_2) decreases. Without an electronic depletion layer, the contact of PCMO at a metal interface is approximately ohmic [24]. In that case, β_1 should be $0\,\mathrm{V}^{-1}$. With higher $|V|$, more traps are ionized, a higher fraction of the depletion layer is ionized and decreases (β_1).

Figure 6(a) shows that -1.4 V is not enough to ionize the traps. However, once the volatile state is excited, the resistance is decreased at $-1.4\,\mathrm{V}$, too. Figures 10(a) and 10(c) show the two states. While in (a) no traps are ionized, (c) shows a finite amount of ionized traps. Two arguments explain the difference of the resistance in the subloop: First, ionizing the traps decreases the resistance of the PCMO more than the resistance of the AlO_x. In turn $|V_1|$ increases and ionizes the traps already at lower $|V|$. Second, the depletion zone width is dependent on the charge states of the traps [41] since charged trap contribute to the screening of the applied electronic potential.

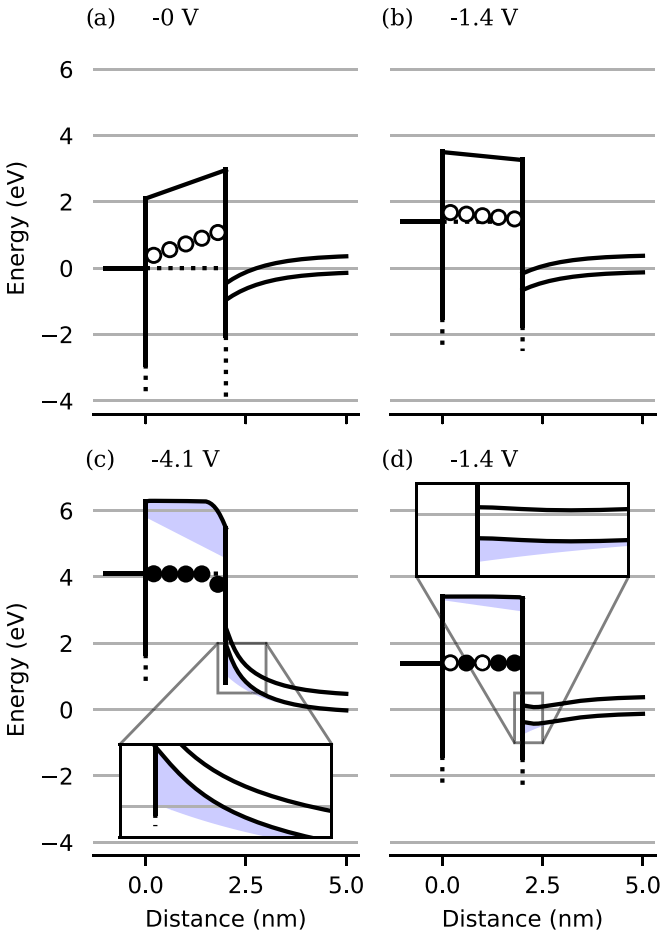

FIG. 10. The LRS band structure in a SC device, without and with excited volatile LRS. The circles represent the traps: empty circles for empty traps, filled circles for charged traps. The difference between the band structure with and without field generated by the charged traps is filled in blue. (a) The band structure at 0 V. (b) Down sweep, $V = -1.4\,\mathrm{V}$ ($V_1 = -1.1\,\mathrm{V}, V_2 = -0.3\,\mathrm{V}$). The traps responsible for the volatile LRS are not yet excited. The traps lie at -1.8 eV below the CB. (c) The maximum voltage, $V = -4.1\,\mathrm{V}$ ($V_1 = -2.1\,\mathrm{V}, V_2 = -2\,\mathrm{V}$). All traps are ionized, and the increased screening shifts the CB and trap band downwards. The traps lie -2.2 eV below the CB. (d) Up sweep, $V = -1.4\,\mathrm{V}$ ($V_1 = -1.2\,\mathrm{V}, V_2 = -0.2\,\mathrm{V}$). The higher voltage drop across the barrier and downshift of the traps by the screening allows the traps to still be ionized. The traps lie at -2 eV.

In summary, electrons injected from the Al electrode charge trap states deep inside the AlO_x bandgap and result in an intermediate volatile LRS.

V. CONCLUSIONS

In this paper, we presented a mathematical model for the Al/PCMO device system with single-crystalline and polycrystalline PCMO. This system has two regions of increased resistance at the interface, namely an insulating AlO_x formed

at the Al/PCMO interface and the resulting oxygen depleted PCMO layer. Moreover, the PCMO layer becomes hole depleted due to the band bending at the interface. We identified these two regions by employing XPS and IS. A simple model of two exponential resistors in series describes the R-V data very well.

The drift and diffusion of oxygen vacancies is responsible for the changes of the resistance in the two regions during switching and relaxation. In particular, oxygen vacancies in the AlO_x decrease its resistance and increase the current flow through traps. Oxygen vacancies in the PCMO increase its resistance, because they break the current carrying paths through the oxygen p orbitals and reduce the number of holes.

The SET and RESET takes place at $V < 0$ and $V > 0$, respectively. The SET only starts for -2 V (-1.6 V) for SC (PC) devices, while the RESET starts directly for $V > 0$ for both devices. Both, an internal voltage between the PCMO and the Al caused by the space charge region and the high oxygen affinity of the Al are responsible for this strong asymmetry.

Polycrystalline samples show a larger difference between the LRS and the HRS and a homogeneous (RE)SET in the fit parameters, while the RE(SET) of the SC devices can be divided into three different regions.

The lower mobility of oxygen vacancies in the SC PCMO create an AlO_x barrier with a lower resistance during the initialization of the device. This reduces the voltage drop over the AlO_x and results in a step-wise (RE)SET: first the oxygen vacancies in the PCMO move and at higher voltage, when the voltage drop over the AlO_x is sufficient, the oxygen vacancies inside the AlO_x move.

Both devices show a volatile LRS. We attribute it to a charging of trap states, which leads to subloops in the IV curves with an slightly higher resistance, which decay within several ms. The decay leads to a LRS compared to the LRS directly after the switching cycle. Nevertheless, LRS and HRS are still distinguishable.

This in-depth analysis of the Al/PCMO system with the mathematical two resistor model provides the basis for future engineering of other barrier/PCMO systems. Our approach offers a simple model, which provides a high flexibility to analyze a wide variety of complex VCM systems and material combinations. Additionally, due to its mathematical simplicity, this model might be employed as compact model for circuit simulations in the future.

ACKNOWLEDGMENTS

We thank our colleague Dr. Carsten Funck for providing insights and expertise on trap states and transport mechanism in oxides that strongly improved the manuscript. This work was supported by the DFG (German Science Foundation) within the collaborative research center SFB 917 “Nanoswitches”, by the Helmholtz Association Initiative and Networking Fund under Project No. SO-092 [Advanced Computing Architectures (ACA)] and the Federal Ministry of Education and Research (Project NEUROTEC, Grants No. 16ME0398K and No. 16ME0399) and NeuroSys as part of the initiative “Clusters4Future” is funded by the Federal Ministry of Education and Research BMBF (03ZU1106AB).

[1] E. W. Lim and R. Ismail, Conduction mechanism of valence change resistive switching memory: A survey, Electronics (Switzerland) **4**, 586 (2015).

[2] D. Ielmini and R. Waser, *Resistive Switching: From Fundamentals of Nanoionic Redox Processes to Memristive Device Applications* (John Wiley, Hoboken, NJ, 2016)

[3] M. Lübben, P. Karakolis, V. Ioannou-Sougleridis, P. Normand, P. Dimitrakis, and I. Valov, Graphene-modified interface controls transition from VCM to ECM switching modes in Ta/TaO_x based memristive Devices, Adv. Mater. **27**, 6202 (2015).

[4] A. Wedig, M. Luebben, D. Y. Cho, M. Moors, K. Skaja, V. Rana, T. Hasegawa, K. K. Adepalli, B. Yildiz, R. Waser, and I. Valov, Nanoscale cation motion in TaO_x, HfO_x, and TiO_x memristive systems, Nat. Nanotechnol. **11**, 67 (2016).

[5] R. Waser, R. Dittmann, C. Staikov, and K. Szot, Redox-based resistive switching memories nanoionic mechanisms, prospects, and challenges, Adv. Mater. **21**, 2632 (2009).

[6] A. Gutsche, S. Siegel, J. Zhang, S. Hambsch, and R. Dittmann, Exploring area-dependent $Pr_{0.7}Ca_{0.3}MnO_3$-based memristive devices as synapses in spiking and artificial neural networks, Front. Neurosci. **15**, 661261 (2021).

[7] B. Arndt, F. Borgatti, F. Offi, M. Phillips, P. Parreira, T. Meiners, S. Menzel, K. Skaja, G. Panaccione, D. A. MacLaren, R. Waser, R. Dittmann *et al.*, Spectroscopic indications of tunnel barrier charging as the switching mechanism in memristive devices, Adv. Funct. Mater. **27**, 1702282 (2017).

[8] D. E. Kwon, J. Kim, Y. J. Kwon, K. S. Woo, J. H. Yoon, and C. S. Hwang, Area-type electronic bipolar resistive switching of Pt/Al_2O_3/Si_3N_3/Ti with forming-free, self-rectification, and nonlinear characteristics, Phys. Status Solidi RRL **14**, 2000209 (2020).

[9] Y. B. Zhu, K. Zheng, X. Wu, and L. K. Ang, Enhanced stability of filament-type resistive switching by interface engineering, Sci. Rep. **7**, 43664 (2017).

[10] F. Pan, C. Chen, Z. S. Wang, Y. C. Yang, J. Yang, and F. Zeng, Nonvolatile resistive switching memories-characteristics, mechanisms and challenges, Prog. Nat. Sci.: Mater. Int. **20**, 1 (2010).

[11] A. Sawa and R. Meyer, Interface type switching, in *Resistive Switching: From Fundamentals of Nanoionic Redox Processes to Memristive Device Applications*, edited by D. I. R. Waser (John Wiley, Hoboken, NJ, 2016).

[12] A. Sawa, T. Fujii, M. Kawasaki, and Y. Tokura, Hysteretic current-voltage characteristics and resistance switching at a rectifying Ti/$Pr_{0.7}Ca_{0.3}MnO_3$ interface, Appl. Phys. Lett. **85**, 4073 (2004).

[13] K. Moon, A. Fumarola, S. Sidler, J. Jang, P. Narayanan, R. M. Shelby, G. W. Burr, and H. Hwang, Bidirectional non-filamentary RRAM as an analog neuromorphic synapse, Part I: Al/Mo/$Pr_{0.7}Ca_{0.3}MnO_3$ material improvements and device measurements, IEEE J. Electron Devices Soc. **6**, 146 (2018).

[14] D.-J. Seong, M. Hassan, H. Choi, J. Lee, J. Yoon, J.-B. Park, W. Lee, M.-S. Oh, and H. Hwang, Resistive-switching characteristics of Al/$Pr_{0.7}Ca_{0.3}MnO_3$ for nonvolatile memory applications, IEEE Electron Device Lett. **30**, 919 (2009).

[15] D.-j. Seong, J. Park, N. Lee, M. Hasan, S. Jung, H. Choi, J. Lee, M. Jo, W. Lee, S. Park, S. Kim, Y. H. Jang, Y. Lee, M. Sung, D. Kil, Y. Hwang, S. Chung, S. Hong, J. Roh, H. Hwang *et al.*, Effect of oxygen migration and interface engineering on resistance switching behavior of reactive metal/polycrystalline $Pr_{0.7}Ca_{0.3}MnO_3$ device for nonvolatile memory applications, in *2009 IEEE International Electron Devices Meeting (IEDM)* (IEEE, 2009), p. 1, doi: 10.1109/IEDM.2009.5424410.

[16] A. Baikalov, Y. Q. Wang, B. Shen, B. Lorenz, S. Tsui, Y. Y. Sun, Y. Y. Xue, and C. W. Chu, Field-driven hysteretic and reversible resistive switch at the Ag-$Pr_{0.7}Ca_{0.3}MnO_3$ interface, Appl. Phys. Lett. **83**, 957 (2003).

[17] Y. B. Nian, J. Strozier, N. J. Wu, X. Chen, and A. Ignatiev, Evidence for an Oxygen Diffusion Model for the Electric Pulse Induced Resistance Change Effect in Transition-Metal Oxides, Phys. Rev. Lett. **98**, 146403 (2007).

[18] W. S. Lau, An extended unified schottky-poole-frenkel theory to explain the current-voltage characteristics of thin film metal-insulator-metal capacitors with examples for various high-k dielectric materials, ECS J. Solid State Sci. Technol. **1**, N139 (2012).

[19] S. D. Ganichev, E. Ziemann, W. Pretll, I. N. Yassievich, A. A. Istratov, and E. R. Weber, Distinction between the Poole-Frenkel and tunneling models of electric-field-stimulated carrier emission from deep levels in semiconductors, Phys. Rev. B **61**, 10361 (2000).

[20] Y. Takeuti and H. Funada, Theory of electron tunneling in semiconductors, J. Phys. Soc. Jpn. **20**, 1854 (1965).

[21] F. Jimenez-Molinos, F. Gamiz, A. Palma, P. Cartujo, and J. Lopez-Villanueva, Direct and trap-assisted elastic tunneling through ultrathin gate oxides, J. Appl. Phys. **91**, 5116 (2002).

[22] F. Jimenez-Molinos, A. Palma, F. Gamiz, J. Banqueri, and J. A. Lopez-Villanueva, Physical model for trap-assisted inelastic tunneling in metal-oxide-semiconductor structures, J. Appl. Phys. **90**, 3396 (2001).

[23] C. C. Wang and L. W. Zhang, Polaron relaxation related to localized charge carriers in $Pr_{1-x}Ca_xMnO_3$, New J. Phys **9**, 210 (2007).

[24] A. Herpers, Electrical characterization of manganite and titanate heterostructures, Ph.D. thesis, RWTH Aachen, 2014.

[25] See Supplemental Material at http://link.aps.org/supplemental/10.1103/PhysRevMaterials.6.095002 for insights into the used pulse scheme, the performed measurements and the crystallographic behaviour of the different samples.

[26] J. Moulder and J. Chastain, *Handbook of X-ray Photoelectron Spectroscopy: A Reference Book of Standard Spectra for Identification and Interpretation of XPS Data* (Physical Electronics Division, Perkin-Elmer Corporation, 1992).

[27] P. van der Heide, *X-ray Photoelectron Spectroscopy: An introduction to Principles and Practices* (John Wiley, Hoboken, NJ, 2011).

[28] E. S. Ilton, J. E. Post, P. J. Heaney, F. T. Ling, and S. N. Kerisit, XPS determination of Mn oxidation states in Mn (hydr)oxides, Appl. Surf. Sci. **366**, 475 (2016).

[29] E. O. Filatova and A. S. Konashuk, Interpretation of the changing the band gap of Al_2O_3 depending on its crystalline form: Connection with different local symmetries, J. Phys. Chem. C **119**, 20755 (2015).

[30] S. Asanuma, H. Akoh, H. Yamada, and A. Sawa, Relationship between resistive switching characteristics and band diagrams of Ti/$Pr_{1-x}Ca_xMnO_3$ junctions, Phys. Rev. B **80**, 235113 (2009).

[31] P. Dimitrakis, *Charge Trapping Non-Volatile Memories—Emerging Materials and Structures*, edited by P. Dimitrakis (Springer, New York, 2017), Vol. 2.

[32] Z. Fan, H. Fan, L. Yang, P. Li, Z. Lu, G. Tian, Z. Huang, Z. Li, J. Yao, Q. Luo *et al.*, Resistive switching induced by charge trapping/detrapping: A unified mechanism for colossal electroresistance in certain Nb:$SrTiO_3$-based heterojunctions, J. Mater. Chem. C **5**, 7317 (2017).

[33] M. D. Murbach, B. Gerwe, N. Dawson-Elli, and L. kun Tsui, impedance.py: A python package for electrochemical impedance analysis, J. Open Source Softw. **5**, 2349 (2020).

[34] T. Nakamura, K. Homma, and K. Tachibana, Thin film deposition of metal oxides in resistance switching devices: Electrode material dependence of resistance switching in manganite films, Nanoscale Res. Lett. **8**, 76 (2013).

[35] D. Deger, K. Ulutas, and S. Yakut, Ac conductivity and dielectric properties of Al_2O_3 thin films, J. Ovonic Res. **8**, 179 (2012).

[36] H. Spahr, S. Montzka, J. Reinker, F. Hirschberg, W. Kowalsky, and H.-H. Johannes, Conduction mechanisms in thin atomic layer deposited Al_2O_3 layers, J. Appl. Phys. **114**, 183714 (2013).

[37] K. Chari and B. Mathur, The conduction properties of anodic Al_2O_3 films, Thin Solid Films **75**, 157 (1981).

[38] E. Cockayne, Influence of oxygen vacancies on the dielectric properties of hafnia: First-principles calculations, Phys. Rev. B **75**, 094103 (2007).

[39] F. Borgatti, C. Park, A. Herpers, F. Offi, R. Egoavil, Y. Yamashita, A. Yang, M. Kobata, K. Kobayashi, J. Verbeeck, G. Panaccione, and R. Dittmann, Chemical insight into electroforming of resistive switching manganite heterostructures, Nanoscale **5**, 3954 (2013).

[40] J. Frenkel, On pre-breakdown phenomena in insulators and electronic semi-conductors, Phys. Rev. **54**, 647 (1938).

[41] J. G. Simmons, Electric tunnel effect between dissimilar electrodes separated by a thin insulating film, J. Appl. Phys. **34**, 2581 (1963).

[42] S. Schramm, J. Hoffmann, and C. Jooss, Transport and ordering of polarons in CER manganites PrCaMnO, J. Phys.: Condens. Matter **20**, 395231 (2008).

[43] C. Pithan (to be published).

[44] R. A. De Souza, Oxygen diffusion in $SrTiO_3$ and related perovskite oxides, Adv. Funct. Mater. **25**, 6326 (2015).

[45] C. La Torre, A. Kindsmüller, D. J. Wouters, C. E. Graves, G. A. Gibson, J. P. Strachan, R. S. Williams, R. Waser, and S. Menzel, Volatile HRS asymmetry and subloops in resistive switching oxides, Nanoscale **9**, 14414 (2017).

[46] O. A. Dicks, J. Cottom, A. L. Shluger, and V. V. Afanas'ev, The origin of negative charging in amorphous Al_2O_3 films: The role of native defects, Nanotechnology **30**, 205201 (2019).

[47] M. Zahid, D. Aguado, R. Degraeve, W. Wang, B. Govoreanu, M. Toledano-Luque, V. Afanas'ev, and J. Van Houdt, Applying complementary trap characterization technique to crystalline γ-phase-Al_2O_3 for improved understanding of nonvolatile memory operation and reliability, IEEE Trans. Electron Devices **57**, 2907 (2010).